Journal of Power Sources 214 (2012) 171–177

Contents lists available at SciVerse ScienceDirect

Journal of Power Sources

journal homepage: www.elsevier.com/locate/jpowsour

$Li_3V_2(PO_4)_3$ nanocrystals embedded in a nanoporous carbon matrix supported on reduced graphene oxide sheets: Binder-free and high rate cathode material for lithium-ion batteries

Xianhong Rui [a,b], Daohao Sim [a], Kangming Wong [a], Jixin Zhu [a], Weiling Liu [a], Chen Xu [a], Huiteng Tan [a], Ni Xiao [a], Huey Hoon Hng [a], Tuti Mariana Lim [b,c,*], Qingyu Yan [a,d,e,*]

[a] School of Materials Science and Engineering, Nanyang Technological University, 639798 Singapore, Singapore
[b] School of Civil and Environmental Engineering, Nanyang Technological University, 639798 Singapore, Singapore
[c] School of Life Sciences and Chemical Technology, Ngee Ann Polytechnic, 599489 Singapore, Singapore
[d] Energy Research Institute, Nanyang Technological University, 637459 Singapore, Singapore
[e] TUM CREATE Centre for Electromobility, Nanyang Technological University, 637459 Singapore, Singapore

HIGHLIGHTS

- Ultrafine $Li_3V_2(PO_4)_3$ nanocrystals (5–8 nm) are synthesized.
- A unique structure is designed by combination of LVP, nanoporous carbon and rGO.
- Binder-free LVP-NC@NPCM@rGO cathode shows excellent Li storage properties.

GRAPHICAL ABSTRACT

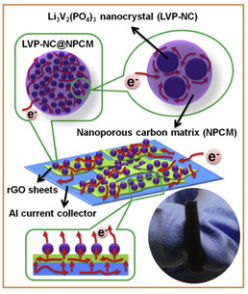

ARTICLE INFO

Article history:
Received 16 February 2012
Received in revised form
26 March 2012
Accepted 31 March 2012
Available online 5 May 2012

Keywords:
Lithium vanadium phosphate
Lithium-ion battery
Nanoporous carbon
Reduced graphene oxide

ABSTRACT

$Li_3V_2(PO_4)_3$ nanocrystals (5–8 nm) embedded in a nanoporous carbon matrix attached onto reduced graphene oxide nanosheets (LVP-NC@NPCM@rGO) are synthesized by a facile approach. The rGO sheets not only form the interconnected conducting scaffold to enhance the charge transfer but also act as the heterogeneous nucleation site to facilitate the growth of nanograins of LVP. The nanoporous carbon acts as the nanocontainer to enhance the electrolyte/active material interaction and also inhibit the grain growth of $Li_3V_2(PO_4)_3$. This leads to the fast kinetics of the Li ion transfer and the excellent cathode performance, especially at high current densities. Binder-free cathodes can be prepared based such LVP-NC@NPCM@rGO sample, which shows high specific capacities, stable cyclabilities and excellent rate capabilities in the voltage ranges of 3.0–4.3 and 3.0–4.8 V.

1. Introduction

The development of safe, high-energy- and power-density, low-cost and long-lasting lithium-ion batteries (LIBs) is of great technological importance for wide spread applications including electric vehicle (EV), renewable energy storage, aerospace and

* Corresponding authors. School of Materials Science and Engineering, Nanyang Technological University, 639798 Singapore, Singapore. Tel.: +65 6790 4583; fax: +65 6790 9081.
E-mail addresses: tmlim@ntu.edu.sg (T.M. Lim), Alexyan@ntu.edu.sg (Q. Yan).

0378-7753/$ – see front matter © 2012 Elsevier B.V. All rights reserved.
doi:10.1016/j.jpowsour.2012.03.113

smart electrical grid [1–3]. Most commercial LIBs use lithium cobalt oxides as the positive electrodes, but there are concerns about its high cost and environmental toxicity. Olivine-type $LiFePO_4$ has emerged as a promising candidate owing to its low price and high safety eventhough it shows a lower Li intercalation voltage (e.g. 3.45 V *vs.* 4 V) and a lower energy density than that of cobalt-based materials [4]. Hence further improvement of such type of cathode materials is encouraged. The higher discharge potential (e.g. 3.6–4.55 V) and higher theoretical capacity (e.g. 197 mAh g^{-1}) of monoclinic $Li_3V_2(PO_4)_3$ (LVP) have triggered significant research efforts [5]. The thermodynamically stable monoclinic LVP phase consists of a three-dimensional (3D) framework of slightly distorted VO_6 octahedra, PO_4 tetrahedra sharing oxygen vertexes (Supporting Information, Fig. S1) [5], corner-shared chains of Li polyhedra and interconnected interstitial space, which leads to a fast ionic transport.

One of the challenges associated with the use of LVP cathodes for high-power LIBs is how to circumvent the limitation of their intrinsically low electronic conductivity ($\sim 10^{-8}$ S cm^{-1}) [6]. Approaches for enhancing electron transport kinetic in batteries include: (1) designing nano-sized electrode materials [5,7–12]. The nanoscale electrodes require short diffusion paths of charge carriers, resulting in a much enhanced power performance. However, obtaining nanostructured LVP is not easy, especially below 10 nm size, due to the uncontrollable crystal growth during the high-temperature treatment (normally between 700 and 900 °C) [13–18]. (2) Coating the active material with a conductive layer, typically carbon [5,19–22]. Inspired by this technique, many efforts have been carried out over the past few years to enhance the rate capability of LVP by thermal decomposition of various carbon-containing precursors, such as glucose [13–15], citric acid [14,16], starch [14], polyethyleneglycol [17], and 1,4-dihydroxy-2-butyne [18], to obtain carbon layers to improve the conductivity of the solid phase. However, this type of approaches normally results in LVP with partial carbon coating and large grain size, (e.g. > 50 nm), which leads to a large polarization of the electrode due to un-optimized electron transport process (Supporting Information, Fig. S2). In addition, it should be noted that LVP contains three mobile Li cations, which allows reversible extraction/insertion of 2.0 Li^+ (or a theoretical capacity of 132 mAh g^{-1}) between 3.0 and 4.3 V. However, when the upper cut-off voltage increases to 4.8 V, full extraction of the third Li^+ is difficult due to extremely sluggish kinetics of both Li^+ and e^- transport in $V_2(PO_4)_3$. For example, the PVDF-mediated LVP delivers 95 mAh g^{-1} at a discharge rate of 5 C between 3 and 4.3 V (e.g. 72% of the theoretical value) but it only delivers 78 mAh g^{-1} at 5 C between 3 and 4.8 V (e.g. only 40% of theoretical capacity, 197 mAh g^{-1}) [14]. Thus, it is of technical challenge to improve the cathode performance of LVP in a wider voltage window (3.0–4.8 V) with a higher theoretical capacity.

Recently, binder-free electrodes have attracted great attention in the development of rollable batteries, which may show enhanced rate capabilities [23–26] and open up the possibility of LIB applications at high temperatures, e.g. > 200 °C, at which most binders are not stable [27]. However, this concept is mainly demonstrated on anodes. On the other hand, there are several reports on novel nanostructures of phosphate-based cathode materials for high-performance LIB applications, e.g. $LiFePO_4$ particles with complete carbon coatings [19], $LiFePO_4$ nanoparticles embedded in a nanoporous carbon matrix [4] and $LiMn_{1-x}Fe_xPO_4$ nanorods on reduced graphene oxide (rGO) sheets [28]. LVP/graphene composites have been prepared [29] and show promising cathode performance (~70 mAh g^{-1} when discharge at 50 C). But the grain size of LVP in the previous study was large (~50 nm) due to less confinement of the grain growth at high synthesis temperatures, e.g. ~800 °C. It is understand that the rate capability is directly related to the kinetics of the Li diffusion in the active materials. Thus, confining the grain size and maximizing the contact area between the electrolyte and active components are the keys to further improve such material for high-power applications including electric vehicles. The nanoporous carbon can act as an electrolyte container [4,30] as well as the template to inhibit the grain growth of inorganic grains during high-temperature process. Combination of LVP nanocrystals, nanoporous carbon and rGO to make high-performance cathode, as illustrated in Scheme 1, is therefore promising.

Herein, we present a facile approach to synthesize 5–8-nm LVP nanocrystals embedded in a nanoporous carbon matrix (LVP-NC@NPCM) attached onto rGO sheets, which is hereafter abbreviated as LVP-NC@NPCM@rGO. The rGO sheets not only form the interconnected conducting scaffold to enhance the charge transfer but also act as the heterogeneous nucleation site to facilitate the growth of nanograins of LVP. The nanoporous carbon acts as the nanocontainer to enhance the electrolyte/active material interaction and also inhibit the grain growth of $Li_3V_2(PO_4)_3$, which leads to the fast kinetics of the Li ion transfer and the excellent cathode performance in both voltage ranges of 3.0–4.3 and 3.0–4.8 V, especially at high current densities. As-prepared LVP-NC@NPCM@rGO composites can be further used to fabricate the binder-free cathode, as illustrated in the insert in Scheme 1. Such cathode shows high specific capacities, stable cyclabilities and excellent rate capabilities e.g. it can be charged or discharged at a high rate of 50 C between 3.0 and 4.3 V with a reversible capacity of ~90 mAh g^{-1}.

2. Experimental

In a typical synthesis, 0.6 mM NH_4VO_3 (Alfa Aesar) was first dissolved in 30 mL of distilled water under vigorous stirring at 60 °C to give a yellow solution. Next, stoichimetric amounts of $CH_3COOLi \cdot 2H_2O$ (Aldrich), $NH_4H_2PO_4$ (Sigma–Aldrich) and 37 mg citric acid (Alfa Aesar) were dissolved in this order into above solution under stirring. This solution was then introduced into 20 mL of graphene oxide (73 mg) dispersion prepared from natural graphite (SP-1) by a modified Hummers method [31–33] and stirred for 12 h at room temperature. Subsequently, the mixture was stirred at 60 °C to remove the excess water so that black gels were obtained. Afterwards, the gel precursors were first heated at 350 °C for 5 h under Ar, followed by milling and then heating at 750 °C for 8 h under Ar containing 5% H_2.

X-ray powder diffraction (XRD) patterns were recorded on a Bruker AXS D8 advance X-ray diffractometer at the 2θ range of 10–60° using Cu Kα radiation. The morphology was investigated by using a field-emission scanning electron microscopy (FESEM) system (JEOL, Model JSM-7600F), and the nanostructure was characterized by using a transmission electron microscopy (TEM) instrument (JEOL, Model JEM-2010 and 2100F) operating at 200 kV. Thermogravimetry analysis was carried out from room temperature to 900 °C at a heating rate of 10 K min^{-1} in air using TGA Model Q500. Raman spectra were obtained by WITec CRM200 confocal Raman microscopy system at a laser wavelength of 488 nm and a spot size of 0.5 mm. Nitrogen adsorption/desorption isotherms were conducted at 77 K (ASAP 2020).

The coin-type cells were assembled in an argon-filled glove-box, where both moisture and oxygen levels were less than 1 ppm. The binder-free cathodes were fabricated as following: (1) depositing the slurry of LVP-NC@NPCM@rGO in ethanol solvent onto the aluminum foils (Ø = 14 mm) without addition of carbon black and PVDF; (2) drying at 70 °C; (3) calendaring under a pressure of about 2 MPa. The mass loading was around 1.0–2.0 mg. Lithium foils were used as anodes and the electrolyte solution was made of 1 M $LiPF_6$

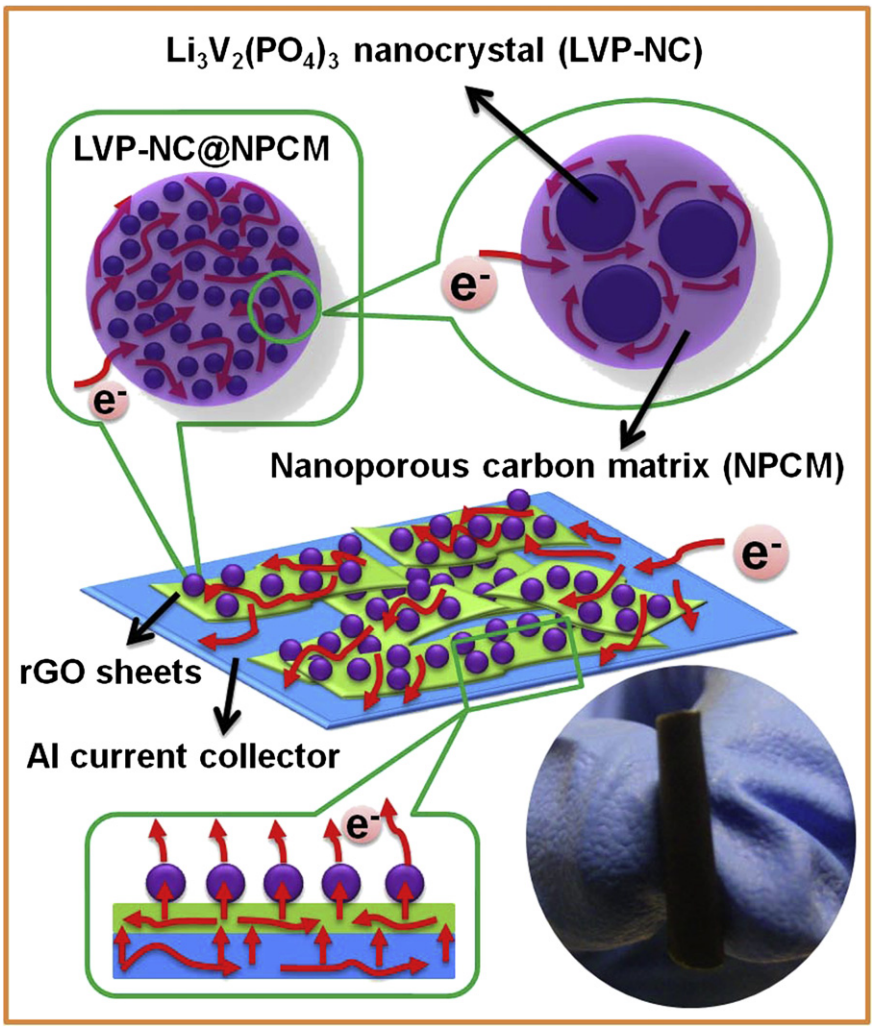

Scheme 1. Designed ideal structure for the composite of LVP nanocrystals embedded in a nanoporous carbon matrix attached onto reduced graphene oxide sheets and its electron-transfer pathways throughout the whole binder-free electrode. Inset: optical image of binder-free LVP-NC@NPCM@rGO electrode.

in ethylene carbonate (EC)/dimethyl carbonate (DMC) (1/1, w/w). The cells were tested on a NEWARE multi-channel battery test system with galvanostatic charge and discharge. Electrochemical impedance spectra (frequency range: 0.001 ~ 10^5 Hz) were performed with an electrochemical workstation (CHI 660C).

3. Results and discussion

The X-ray diffraction (XRD) pattern of the as-obtained LVP-NC@NPCM@rGO sample is shown in Fig. 1a. Besides the diffraction peaks of monoclinic $Li_3V_2(PO_4)_3$ (space group: $P2_1/n$ (14), ICSD #96962) [15], an additional diffraction shoulder peak at $2\theta = 25°$, partially overlapping with the LVP (121) peak, originates from the stacked graphene sheets in LVP-NC@NPCM@rGO. No obvious peaks corresponding to graphite are found in the XRD pattern, indicating the carbon in the sample is not well crystallized. There are no detectable crystalline impurities as indicated by the XRD pattern. Fig. 1b shows the Raman spectra of LVP-NC@NPCM@rGO, the reference GO sample and the carbon coated LVP (LVP/C) sample prepared in the absent of GO. The Raman spectrum of LVP-NC@NPCM@rGO displays two characteristic bands of carbonaceous materials located at 1361 cm^{-1} (D-band, disorder-induced phonon mode) and at 1595 cm^{-1} (G-band, graphite band), which may be a mixed signals from both amorphous carbon and rGO sheets. Meanwhile, the four-point-probe measurements show that the electrical conductivities of LVP-NC@NPCM@rGO and LVP/C are 330 and 11 S m^{-1}, respectively, while GO is electrically insulating, which indicates that the GO is successfully reduced in the annealing process. Based on the thermogravimetric analysis (TGA) result (Supporting Information, Fig. S3), the total content of carbon materials, including both rGO and amorphous carbon, in LVP-NC@NPCM@rGO is calculated to be 29.0 wt% while the content of amorphous carbon in LVP/C sample is 11.9 wt%.

The morphology of the LVP-NC@NPCM@rGO was investigated by field-emission scanning electron microscopy (FESEM) and transmission electron microscopy (TEM), which reveal that quasi-spherical particles with a size of 20–80 nm are uniformly anchored onto the surface of nanosheets (Fig. 2a–b). The selected area electron diffraction (SAED) pattern (inset in Fig. 2b) of the nanosheets shows hexagonal symmetric spots, which confirms the presence of graphene. The high-magnification TEM image (Fig. 2c) of a single nanoparticle displays that it consists of nanograins with sizes in the range of 5–8 nm embedded in an amorphous matrix, which is indicated by the diffused rings in the corresponding SAED pattern (inset in Fig. 2c). The amorphous matrix is believed to be carbon while the high-resolution (HR) TEM image (Fig. 2d) indicates that the carbon matrix is nanoporous with pore sizes of ~ 4 nm. The HRTEM analysis (Fig. 2d–e) further confirms that the

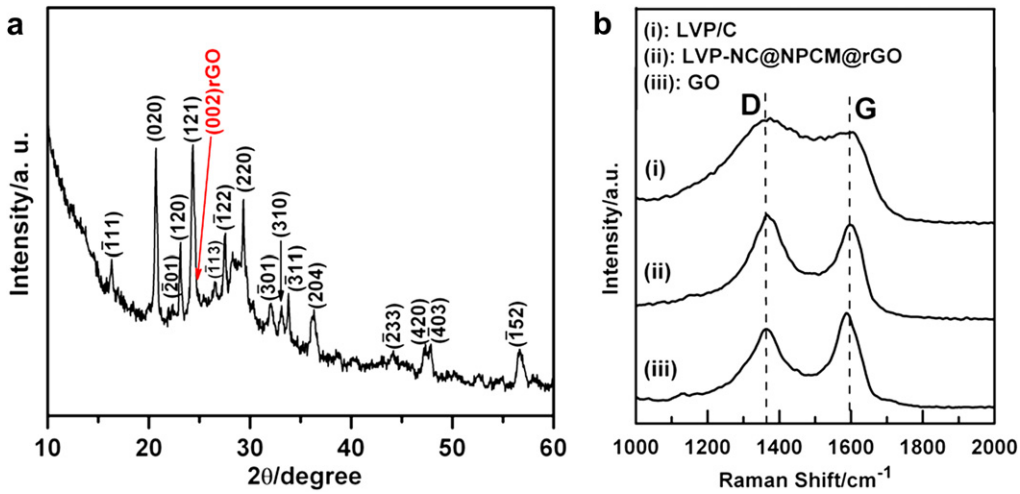

Fig. 1. (a) XRD pattern of the as-prepared LVP-NC@NPCM@rGO. (b) Raman spectra of LVP-NC@NPCM@rGO, reference GO and LVP/C samples.

nanograins in the carbon matrix are monoclinic LVP (ICSD #96962). The observed lattice fringes with a spacing of 0.36 nm (Fig. 2e) correspond to the (121) planes of monoclinic LVP. In comparison, samples prepared without addition of graphene oxides in the precursors are irregular shaped particles with sizes of 1–2 μm (Supporting Information, Fig. S4a). The TEM images (Supporting Information, Fig. S4b–d) reveal that the samples are composed of large LVP grains of 100–500 nm attached in the carbon matrix. The nitrogen adsorption–desorption isotherms of LVP-NC@NPCM@rGO (Fig. 2f) and LVP/C (Supporting Information, Fig. S5) samples show a type IV characteristic, which indicates the presence of mesopores and is consistent with the HRTEM observation (Fig. 2d). Based on the Barrett–Joyner–Halenda (BJH) analysis, the pore-size distribution (insets in Fig. 2f and Fig. S5) is narrow with an average size of 3.3 nm for both samples. The specific surface area is estimated to be ~156 m^2 g^{-1} for LVP/C@rGO and ~27 m^2 g^{-1} for LVP/C,

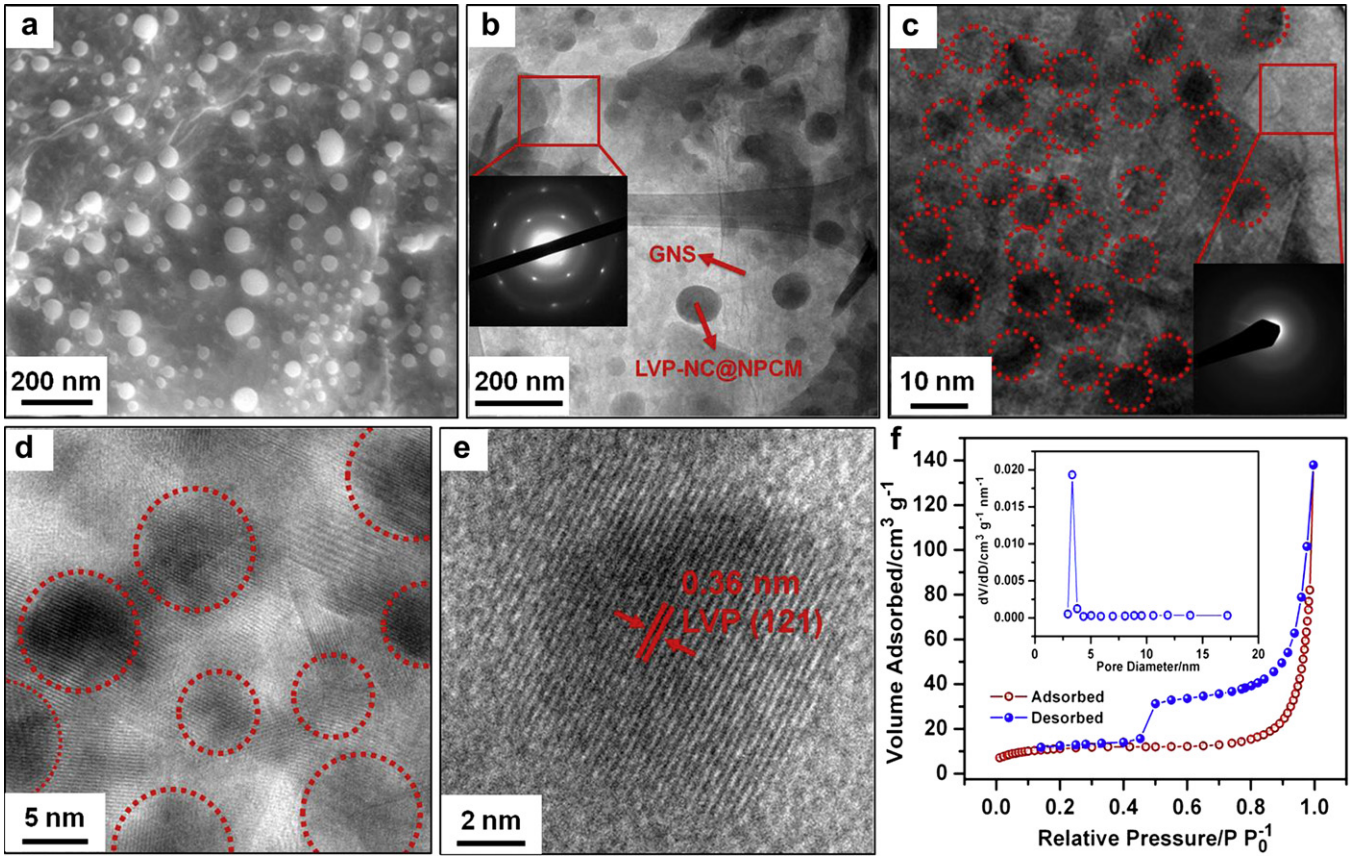

Fig. 2. (a) FESEM and (b) TEM images of LVP-NC@NPCM@rGO. Inset in (b) is the SAED pattern of rGO sheets. (c) High-magnification TEM and (d) HRTEM images of a single nanoparticle, showing that LVP nanocrystals with sizes of 5–8 nm embedded in a nanoporous carbon matrix. Inset in (c) is the SAED of the amorphous carbon. (e) HRTEM image of a single LVP nanocrystal. (f) Nitrogen adsorption/desorption isotherms of LVP-NC@NPCM@rGO. Inset in (f) is the pore-size distribution plot calculated by the BJH formula based on the desorption branch isotherm.

respectively, using the Brunauer–Emmett–Teller (BET) method. The higher specific surface area of LVP-NC@NPCM@rGO sample than that of LVP/C is due to the extra contribution of rGO sheets.

The proposed formation scheme of hierarchical LVP-NC@NPCM@rGO nanoarchitectures is plotted (Supporting Information, Fig. S6). When added to a solution containing VO_2^+, Li^+ and $H_2PO_4^-$ ions, the citric acid (denoted as CA) acts as a chelating agent. The CA molecule can easily capsulate VO_2^+ to form [$CAVO_2^+$] and further combines with Li^+ and $H_2PO_4^-$ to assemble into the structure [$CAVO_2^+\cdots HPO_4^{2-}Li^+$], which is similar as those reported in preparation of $Li_3Fe_2(PO_4)_3$ using a cationic surfactant [34] and CA-mediated $LiFePO_4$ [35]. When GO aqueous suspension is added, the hydroxyl, epoxide and carboxyl groups on the GO sheets act as the heterogeneous nucleation sites to anchor the [$CAVO_2^+\cdots HPO_4^{2-}Li^+$] molecules. The subsequent heat treatments under Ar/H_2 atmosphere led to (1) the formation of LVP nanograins through reduction of VO_2^+, (2) carbonization of CA and (3) the reduction of GO, which result in the hierarchical LVP-NC@NPCM@rGO nanoarchitectures. The presence of the rGO sheets can also help to separate the LVP grains and prevent the coarsening of LVP@NPCM during the heat treatment process.

The presence of rGO sheets in the LVP-NC@NPCM@rGO sample enable the preparation of binder-free cathode by depositing directly the slurry of LVP-NC@NPCM@rGO in *n*-methyl-2-pyrrolidone (NMP) onto the aluminum current collector with a diameter of 14 mm (inset in Scheme 1). For comparison purpose, we also prepared the cathode using LVP/C sample with the addition of 10 wt% PVDF as the binder and 10 wt% carbon black as the conductive phase. The Li storage properties of the LVP-NC@NPCM@rGO binder-free cathode and LVP/C normal cathode were tested in coin-type half cells using lithium foils as the anode [36–38]. Here, it is worth pointing out that the capacity contribution from the carbon matrix or rGO is negligible in the voltage ranges of 3.0–4.3 and 3.0–4.8 V (*vs.* Li^+/Li). Thus, only the mass of LVP was included during the calculation of specific capacities. Fig. 3a shows the galvanostatic charge (Li^+ extraction) and discharge (Li^+ insertion) voltage profiles of the LVP/C and binder-free LVP-NC@NPCM@rGO electrodes at a current density of 66 mA g^{-1} (0.5 C) between 3.0 and 4.3 V. Three typical plateaus are observed at around 3.6, 3.7 and 4.1 V in the charge curves, which correspond to a series of phase transitions of crystalline LVP. The electrochemical reactions are written as [5,39,40]:

$$Li_3V_2(PO_4)_3 - 0.5Li^+ - 0.5e^- \leftrightarrow Li_{2.5}V_2(PO_4)_3 \quad (1)$$

$$Li_{2.5}V_2(PO_4)_3 - 0.5Li^+ - 0.5e^- \leftrightarrow Li_2V_2(PO_4)_3 \quad (2)$$

$$Li_2V_2(PO_4)_3 - 1.0Li^+ - 1.0e^- \leftrightarrow Li_1V_2(PO_4)_3 \quad (3)$$

The two plateaus in the voltage range of 3.6–3.7 V correspond to the reactions (1) and (2). The plateau at 4.1 V is ascribed to a further lithium extraction from $Li_2V_2(PO_4)_3$ (reaction (3)). These reactions are reversible in the subsequent discharge process. As shown in Fig. 3a, the LVP-NC@NPCM@rGO and LVP/C electrodes depict initial charge capacities of 130 and 129 mAh g^{-1} and subsequent discharge capacities of 128 and 125 mAh g^{-1}, respectively, which are close to the theoretical capacity of LVP in this voltage window (132 mAh g^{-1}). Both types of electrodes exhibit excellent cycling stabilities with almost no capacity fading during 100 cycles (Fig. 3b). Relatively higher specific capacities of LVP-NC@NPCM@rGO electrode may be due to the higher activity of fine LVP nanograins (e.g. 5–8 nm).

The cycling responses of the LVP-NC@NPCM@rGO and LVP/C electrodes at different C rates were also evaluated and shown in Fig. 3c. The binder-free LVP-NC@NPCM@rGO electrode shows discharge capacities of 127, 126, 125, 121, 117, 112, 107 and

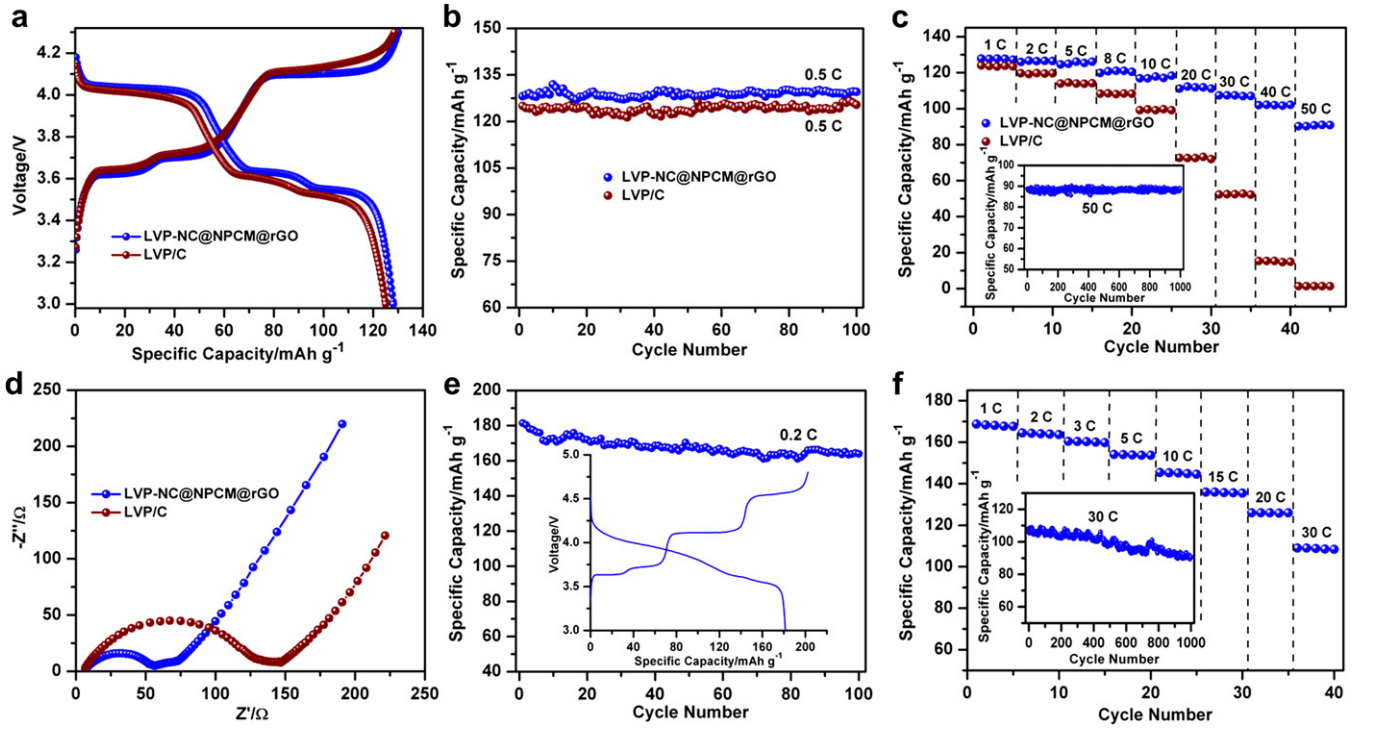

Fig. 3. Electrochemical characterization of binder-free LVP-NC@NPCM@rGO and normal LVP/C electrodes. (a) Initial charge-discharge profiles and (b) cycling performance at a charge/discharge rate of 0.5 C between 3.0 and 4.3 V. (c) Comparison of discharge capacities of two electrodes at various current densities between 3.0 and 4.3 V and (d) the corresponding electrochemical impedance spectra measured at the 4th fully discharged state. Inset in (c) is the cycling performance of LVP-NC@NPCM@rGO electrode at 50 C in the voltage windows of 3.0–4.3 V. (e) Cycling performance at 0.2 C (inset in (e): initial charge/discharge profiles) and (f) rate capability of binder-free LVPNC@ NPCM@rGO electrode in a wider voltage window (3.0–4.8 V). Inset in (f) is the cycling performance of LVP-NC@NPCM@rGO electrode at 30 C in the wider voltage window of 3.0–4.8 V.

102 mAh g^{-1} during the 2nd cycle at current densities of 132 (1 C), 264 (2 C), 660 (5 C), 1056 (8 C), 1320 (10 C), 2640 (20 C), 3960 (30 C) and 5280 mA g^{-1} (40 C), respectively. Even at a very high current density of 6600 mA g^{-1} (50 C), it can still deliver a high capacity of 90 mAh g^{-1}. Such high-C-rate performance of LVP-NC@NPCM@rGO electrode is much better than that of LVP/C electrode, which only achieves low discharge capacities of 52 and 15 mAh g^{-1} at 30 C and 40 C, respectively, and even cannot be discharged at a high rate of 50 C. The inferior Li storage property of LVP/C is mainly attributed to its low electrical conductivity as verified by the electrochemical impedance spectra (Fig. 3d). The LVP/C cathode shows a larger radius of semi-circle in the Nyquist plots as compared to that of the LVP-NC@NPCM@rGO cathode, which indicates a higher charge transfer resistance. Moreover, the LVP-NC@NPCM@rGO electrode exhibits an excellent cyclability at a high rate of 50 C as shown in the inset of Fig. 3c, delivering a discharge capacity of 88 mAh g^{-1} during the 1000th cycle. Such cyclability is comparable to ever-reported high-performance cathodes, such as binder-free layered $LiNi_{0.4}Mn_{0.4}Co_{0.2}O_2$ electrode composed of 5 wt.% single-walled carbon nanotubes [26].

It is known that there is additional Li^+ extraction, associated with the V^{4+}/V^{5+} redox couple, occurring at ~4.6 V plateau. This increases the voltage range to 3.0–4.8 V, leading to a higher theoretical capacity of 197 mAh g^{-1} for LVP. However, this Li^+ extraction at ~4.6 V is kinetically difficult to achieve due to the reduced ionic/electronic conductivity of complete delithiation phase $V_2(PO_4)_3$ [39]. Thus, we also evaluated the electrochemical performance of LVP-NC@NPCM@rGO electrode at 3.0–4.8 V (Fig. 3e, f). The plateau at ~4.6 V (inset in Fig. 3e) can be clearly observed. Importantly, the lithium reinsertion process gives rise to a solid solution behavior ($V_2(PO_4)_3 \rightarrow Li_2V_2(PO_4)_3$) as indicated by the characteristic S-shaped, meaning that Li ions are disordered in the framework. After this point, two-phase transition reappears. The initial discharge capacity of LVP-NC@NPCM@rGO electrode between 3.0 and 4.8 V is as high as 181 mAh g^{-1} with a Coulombic efficiency of 90% at a current density of 40 mA g^{-1} (0.2 C). Although slightly decreased, the reversible discharge capacity still can reach 164 mAh g^{-1} during the 100th cycle, which is much better than those ever-reported for LVP-based cathodes [13–18,29]. Fig. 3f shows the high-C-rate performance of LVP-NC@NPCM@rGO between 3.0 and 4.8 V, which delivers discharge capacities of 168, 164, 160, 154, 145, 136, 126 and 109 mAh g^{-1} during the 2nd cycle at current densities of 197 (1 C), 394 (2 C), 591 (3 C), 985 (5 C), 1970 (10 C), 2955 (15 C), 3940 (20 C) and 5910 mA g^{-1} (30 C), respectively. A superior cycling performance at 30 C can also be achieved in such wider voltage window (inset in Fig. 3f), showing a discharge capacity of 91 mAh g^{-1} during the 1000th cycle. The outstanding Li storage performance of LVP-NC@NPCM@rGO is believed to result from the following aspects: (1) ultrafine LVP nanocrystals (5–8 nm) provide short diffusion distances for Li^+ intercalation/deintercalation; (2) the nanoporous carbon matrix acts as both conducting 3D networks and electrolyte containers to allow fast migration of both Li^+ and e^- to each LVP nanoparticle, which also provides an elastic buffer to maintain structural integrity during repeated charge–discharge processes; (3) highly conductive rGO sheets facilitate the fast charge transfer within the electrode and to the current collector; (4) the binder-free fabrication further improves the electrical conductivity and electrolyte permeation in the LVP-NC@NPCM@rGO electrode.

4. Conclusions

In summary, LVP nanocrystals (5–8 nm) embedded in a nanoporous carbon matrix attached onto rGO nanosheets have been successfully synthesized by combining sol-gel process and high-temperature annealing. The rGO sheets not only form the interconnected conducting scaffold to enhance the charge transfer but also act as the heterogeneous nucleation site to facilitate the growth of nanograins of LVP. The nanoporous carbon acts as the nanocontainer to enhance the electrolyte/active material interaction and also inhibit the grain growth of LVP. Binder-free cathodes can be fabricated based on such LVP-NC@NPCM@rGO sample, which shows high specific capacities, stable cyclabilities and excellent rate capabilities in the voltage ranges of both 3.0–4.3 and 3.0–4.8 V. For example, the composite exhibits a capacity of 90 mAh g^{-1} even at a high rate of 50 C between 3.0 and 4.3 V, which can be remained at 88 mAh g^{-1} after 1000 cycles. For a large voltage window (3.0–4.8 V), the electrode can still deliver high capacities of 168, 145 and 109 mAh g^{-1} at rates of 1, 10 and 30 C, respectively. Combined with a good electrochemical performance and ease of synthesis, LVP-NC@NPCM@rGO can be a very promising cathode material for higher energy density and power demanding lithium-ion batteries.

Acknowledgments

The authors gratefully acknowledge AcRF Tier 1 RG 31/08 of MOE (Singapore), NRF2009EWT-CERP001-026 (Singapore), Singapore Ministry of Education (MOE2010-T2-1-017), A*STAR SERC grant 1021700144 and Singapore MPA 23/04.15.03 RDP 009/10/102 and MPA 23/04.15.03 RDP 020/10/113 grant.

Appendix A. Supplementary material

Supplementary data associated with this article can be found, in the online version, at doi:10.1016/j.jpowsour.2012.03.113.

References

[1] H.G. Zhang, X.D. Yu, P.V. Braun, Nat. Nanotechnol. 6 (2011) 277.
[2] A. Magasinski, P. Dixon, B. Hertzberg, A. Kvit, J. Ayala, G. Yushin, Nat. Mater. 9 (2010) 353.
[3] Y.K. Sun, S.T. Myung, B.C. Park, J. Prakash, I. Belharouak, K. Amine, Nat. Mater. 8 (2009) 320.
[4] X.L. Wu, L.Y. Jiang, F.F. Cao, Y.G. Guo, L.J. Wan, Adv. Mater. 21 (2009) 2710.
[5] H. Huang, S.C. Yin, T. Kerr, N. Taylor, L.F. Nazar, Adv. Mater. 14 (2002) 1525.
[6] S.C. Yin, P.S. Strobel, H. Grondey, L.F. Nazar, Chem. Mater. 16 (2004) 1456.
[7] P.G. Bruce, B. Scrosati, J.M. Tarascon, Angew. Chem. Int. Ed. 47 (2008) 2930.
[8] A.S. Arico, P. Bruce, B. Scrosati, J.M. Tarascon, W.V. Schalkwijk, Nat. Mater. 4 (2005) 366.
[9] X.H. Rui, D.H. Sim, C. Xu, W.L. Liu, H.T. Tan, K.M. Wong, H.H. Hng, T.M. Lim, Q.Y. Yan, RSC Adv. 2 (2012) 1174.
[10] H. Cheng, Z.G. Lu, J.Q. Deng, C.Y. Chung, K.L. Zhang, Y.Y. Li, Nano Res. 3 (2010) 895.
[11] X.J. Zhang, W.H. Shi, J.X. Zhu, W.Y. Zhao, J. Ma, S. Mhaisalkar, T.L. Maria, Y.H. Yang, H. Zhang, H.H. Hng, Q.Y. Yan, Nano Res. 3 (2010) 643.
[12] J.X. Zhu, Z.Y. Yin, H. Li, H.T. Tan, C.L. Chow, H. Zhang, H.H. Hng, J. Ma, Q.Y. Yan, Small 7 (2011) 3458.
[13] M.M. Ren, Z. Zhou, X.P. Gao, W.X. Peng, J.P. Wei, J. Phys. Chem. C 112 (2008) 5689.
[14] X.H. Rui, C. Li, C.H. Chen, Electrochim. Acta 54 (2009) 3374.
[15] P. Fu, Y.M. Zhao, X.N. An, Y.Z. Dong, X.M. Hou, Electrochim. Acta 52 (2007) 5281.
[16] Q.Q. Chen, J.M. Wang, Z. Tang, W.C. He, H.B. Shao, J.Q. Zhang, Electrochim. Acta 52 (2007) 5251.
[17] C.X. Chang, J.F. Xiang, X.X. Shi, X.Y. Han, L.J. Yuan, J.T. Sun, Electrochim. Acta 53 (2008) 2232.
[18] Y.Q. Qiao, J.P. Tu, X.L. Wang, D. Zhang, J.Y. Xiang, Y.J. Mai, C.D. Gu, J. Power Sources 196 (2011) 7715.
[19] X.H. Xia, J.P. Tu, J. Zhang, X.H. Huang, X.L. Wang, W.K. Zhang, H. Huang, Electrochem. Commun. 10 (2008) 1815.
[20] X.H. Rui, Y. Jin, X.Y. Feng, L.C. Zhang, C.H. Chen, J. Power Sources 196 (2011) 2109.
[21] X.H. Rui, N. Yesibolati, C.H. Chen, J. Power Sources 196 (2011) 2279.
[22] X.H. Rui, C. Li, J. Liu, T. Cheng, C.H. Chen, Electrochim. Acta 55 (2010) 6761.
[23] C.M. Ban, Z.C. Wu, D.T. Gillaspie, L. Chen, Y.F. Yan, J.L. Blackburn, A.C. Dillon, Adv. Mater. 22 (2010) E145.
[24] I. Lahiri, S.W. Oh, J.Y. Hwang, S. Cho, Y.K. Sun, R. Banerjee, W. Choi, ACS Nano 4 (2010) 3440.

[25] X.H. Rui, J.X. Zhu, W.L. Liu, H.T. Tan, D.T. Sim, C. Xu, H. Zhang, J. Ma, H.H. Hng, T.M. Lim, Q.Y. Yan, RSC Adv. 1 (2011) 117.
[26] C.M. Ban, Z. Li, Z.C. Wu, M.J. Kirkham, L. Chen, Y.S. Jung, E.A. Payzant, Y.F. Yan, M.S. Whittingham, A.C. Dillon, Adv. Energy Mater. 1 (2011) 58.
[27] B.J. Landi, M.J. Ganter, C.D. Cress, R.A. DiLeo, R.P. Raffaelle, Energy Environ. Sci. 2 (2009) 638.
[28] H.L. Wang, Y. Yang, Y.Y. Liang, L.F. Cui, H.S. Casalongue, Y.G. Li, G.S. Hong, Y. Cui, H.J. Dai, Angew. Chem. Int. Ed. 50 (2011) 7364.
[29] H.D. Liu, P. Gao, J.H. Fang, G. Yang, Chem. Commun. 47 (2011) 9110.
[30] Y.S. Hu, P. Adelhelm, B.M. Smarsly, S. Hore, M. Antonietti, J. Maier, Adv. Funct. Mater. 17 (2007) 1873.
[31] W.S. Hummers, R.E. Offeman, J. Am. Chem. Soc. 80 (1958) 1339.
[32] X.H. Rui, J.X. Zhu, D.H. Sim, C. Xu, Y. Zeng, H.H. Hng, T.M. Lim, Q.Y. Yan, Nanoscale 3 (2011) 4752.
[33] C.X. Guo, M. Wang, T. Chen, X.W. Lou, C.M. Li, Adv. Energy Mater. 1 (2011) 736.
[34] S.M. Zhu, H.S. Zhou, T. Miyoshi, M. Hibino, I. Honma, M. Ichihara, Adv. Mater. 16 (2004) 2012.
[35] J.F. Ni, M. Morishita, Y. Kawabe, M. Watada, N. Takeichi, T. Sakai, J. Power Sources 195 (2010) 2877.
[36] S. Saadat, J. Zhu, M.M. Shahjamali, S. Maleksaeedi, Y.Y. Tay, B.Y. Tay, H.H. Hng, J. Ma, Q. Yan, Chem. Commun. 47 (2011) 9849.
[37] J. Zhu, K. Sun, D. Sim, C. Xu, H.H. Hng, Q. Yan, Chem. Commun. 47 (2011) 10383.
[38] X.H. Rui, N. Yesibolati, S.R. Li, C.C. Yuan, C.H. Chen, Solid State Ionics 187 (2011) 58.
[39] S.C. Yin, H. Grondey, P. Strobel, M. Anne, L.F. Nazar, J. Am. Chem. Soc. 125 (2003) 10402.
[40] S.C. Yin, H. Grondey, P. Strobel, H. Huang, L.F. Nazar, J. Am. Chem. Soc. 125 (2003) 326.